

Understanding Gas Storage in Cuboctahedral Porous Coordination Cages

Gregory R. Lorz,†,‡,|| Eric J. Gosselin,†,|| Benjamin A. Trump,⊥ Arthur H. P. York,¶ Arni Sturluson,¶ Casey A. Rowland,† Glenn P. A. Yap,† Craig M. Brown,§,⊥ Cory M. Simon,¶ and Eric D. Bloch*,†,‡,⊥

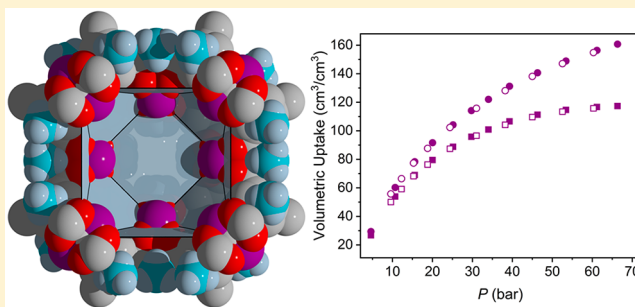
†Department of Chemistry and Biochemistry, ‡Center for Neutron Science, and §Department of Chemical and Biomolecular Engineering, University of Delaware, Newark, Delaware 19716, United States

⊥Center for Neutron Research, National Institute of Standards and Technology, Gaithersburg, Maryland 20899, United States

¶School of Chemical, Biological, and Environmental Engineering, Oregon State University, Corvallis, Oregon 97331, United States

Supporting Information

ABSTRACT: Porous molecular solids are promising materials for gas storage and gas separation applications. However, given the relative dearth of structural information concerning these materials, additional studies are vital for further understanding their properties and developing design parameters for their optimization. Here, we examine a series of isostructural cuboctahedral, paddlewheel-based coordination cages, $M_{24}(\text{}^t\text{Bu-bdc})_{24}$ ($M = \text{Cr, Mo, Ru}$; $\text{}^t\text{Bu-bdc}^{2-} = 5\text{-tert-butylisophthalate}$), for high-pressure methane storage. As the decrease in crystallinity upon activation of these porous molecular materials precludes diffraction studies, we turn to a related class of pillared coordination cage-based metal–organic frameworks, $M_{24}(\text{Me-bdc})_{24}(\text{dabco})_6$ ($M = \text{Fe, Co}$; $\text{Me-bdc}^{2-} = 5\text{-methylisophthalate}$; $\text{dabco} = 1,4\text{-diazabicyclo}[2.2.2]\text{-octane}$) for neutron diffraction studies. The five porous materials display BET surface areas from 1057–1937 m^2/g and total methane uptake capacities of up to 143 $\text{cm}^3(\text{STP})/\text{cm}^3$. Both the porous cages and cage-based frameworks display methane adsorption enthalpies of -15 to -22 kJ/mol . Also supported by molecular modeling, neutron diffraction studies indicate that the triangular windows of the cage are favorable methane adsorption sites with $\text{CD}_4\text{-arene}$ interactions between 3.7 and 4.1 Å. At both low and high loadings, two additional methane adsorption sites on the exterior surface of the cage are apparent for a total of 56 adsorption sites per cage. These results show that $M_{24}L_{24}$ cages are competent gas storage materials and further adsorption sites may be optimized by judicious ligand functionalization to control extracage pore space.



INTRODUCTION

Three-dimensional porous materials have been widely investigated for gas storage applications. Although these have included carbon dioxide,¹ oxygen,² ammonia,³ acetylene,⁴ sulfur dioxide,⁵ ethylene oxide,⁶ ethylene,⁷ and nitrogen,⁸ they have most commonly been studied for the high-pressure storage of small molecules of consequence to energy.⁹ Indeed, the storage of hydrogen^{10–12} and methane^{13–15} in metal–organic frameworks (MOFs) has been the topic of recent review articles. In the case of the former, many metal–organic frameworks have displayed high H_2 storage capacities at cryogenic temperatures, although these are greatly diminished near 298 K. Methane storage capacities approaching U.S. Department of Energy (DOE) targets have been recently reported for a number of metal–organic frameworks.¹⁶ When considering the deliverable capacities of these materials, along with their actual densities (as opposed to crystallographic densities, which are often utilized for total adsorption calculations), MOF capacities fall significantly short of targets.¹⁷ Although flexible MOFs have been touted as a

means to elevate deliverable capacities of these materials,¹⁵ (i) flexible frameworks also suffer from a large discrepancy between bulk and crystallographic density and (ii) a complicated tank design is required to accommodate their dramatic expansion/collapse.¹⁸ However, it is clear that significantly altered strategies must be employed to meet storage and delivery targets. Molecular adsorbents may show utility in this regard, as they offer novel strategies for precise pore design and enhanced control over crystallite size and morphology.¹⁹

Porous molecular solids have shown considerable promise for gas separation,²⁰ catalysis,²¹ chiral separations,²² sensing,²³ and as soluble designer pores for porous liquids.²⁴ In addition to the benefits of three-dimensionally connected porous materials, molecular solids have the additional advantage of solubility and significantly increased molecular-level control. These can aid in the design, synthesis, characterization, and

Received: June 1, 2019

Published: July 4, 2019

utilization of these adsorbents. However, understanding and optimizing porosity in these solids can be challenging, as it can exist as a result of surface area intrinsic to the individual molecule or can arise from void space present from inefficient packing of molecules that need not display porosity.²⁵ Regardless, molecular materials have displayed BET surface areas in excess of 3500 m²/g.²⁶ All-organic porous molecules encompass various molecular species; the organic molecule to first display porosity was Dianin's compound (4-*p*-hydroxyphenyl-2,2,4-trimethylchroman).²⁷ Similarly, calixarenes,²⁸ cucurbiturils,²⁹ Noria,³⁰ phthalocyanines,³¹ boronic ester cages,³² alkyne-based cages,³³ and imine-based cages have all shown considerable porosity.³⁴ Hybrid metal organic cages, also known as metal–organic polyhedra,¹⁹ have been shown to adopt analogous structures, such as octahedral and cuboctahedral cages (Figure 1), but have displayed relatively limited

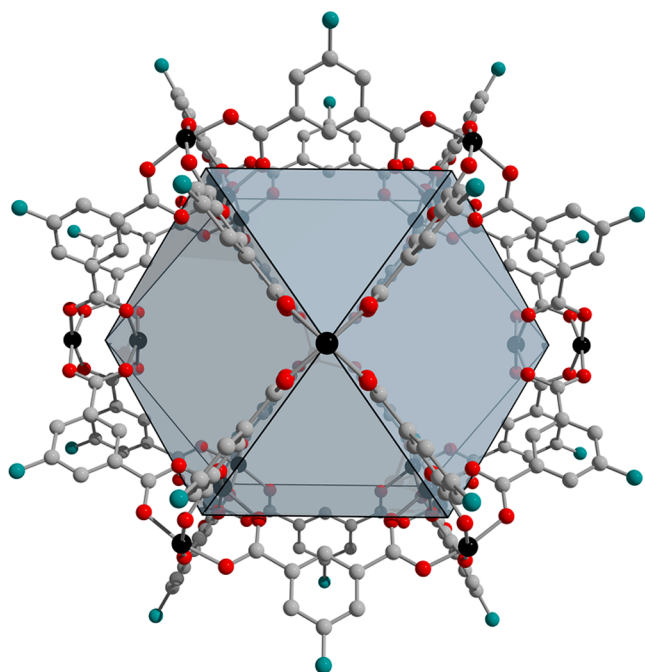


Figure 1. $M_{24}(R\text{-}bdc)_{24}$ cuboctahedral cage featuring bimetallic paddlewheel units. This pore structure, which is isolable as a molecular species, is also pervasive in isophthalic acid-based MOFs. Black, gray, and red spheres represent metal (M), carbon, and oxygen atoms, respectively. The blue spheres represent functional groups (R) that can include hydroxy, alkyl, amino, and others.

porosity.^{35–37} We aim to both expand the scope of porous metal–organic molecular materials and utilize spectroscopic, computational, and diffraction methods to better understand adsorption phenomena in them. In addition to the benefits of porous molecules mentioned above, the cation sites in hybrid metal–organic porous molecules could serve as sites for selective gas adsorption, gas storage, small-molecule activation, or redox chemistry.

Some coordination cages have shown moderate levels of porosity, but the most widely studied have been based on bimetallic paddlewheel building blocks. This is likely a result of the relative ease with which paddlewheel-based materials assemble and their compatibility with a wide variety of ligand functional groups. Indeed, in the vast area of metal–organic frameworks, a very large number of paddlewheel-based MOFs have been reported, from one- to two- to three-dimensional

frameworks.³⁸ For porous coordination cages, paddlewheel building units often assemble into cuboctahedral and octahedral structures. These have been reported for a variety of transition metal cations and ligand functional groups. Cuboctahedral cages are an intriguing set of compounds, as they have been isolated for Cr, Ni, Cu, Mo, Ru, and Rh.^{39–44} Although some of these materials have been reported to possess high surface areas, specifically $Cr_{24}(t\text{-}Bu\text{-}bdc)_{24}$ ($t\text{-}Bu\text{-}bdc^{2-} = 5\text{-}tert\text{-}butylisophthalate$) with a BET surface area of 1135 m²/g,⁴⁵ porosity is often overlooked in coordination cages. Relatedly, there is a lack of structural studies on porous cages upon activation or gas adsorption.

Adsorption properties of porous cages can be partially inferred from analogous metal–organic frameworks, as the cuboctahedral cage serves as the building block for many well-known MOFs. For example, one of three pore types in the canonical MOF, HKUST-1, is a cuboctahedral cage.⁴⁶ Showing the versatility of paddlewheel building units, HKUST-1 analogues have been prepared using a wide variety of transition metal cations including Cr, Fe, Co, Ni, Cu, Zn, Mo, and Ru.⁴⁷ Many of the members of the PCN and NOTT/MFM families of frameworks similarly contain copper paddlewheel-based cuboctahedral pores, including PCN-11,⁴⁸ -12,⁴⁹ and -61⁵⁰ as well as NOTT/MFM-112,⁵¹ -115,⁵² -122⁵³ (also known as NU-125),⁵⁴ and -132.⁵⁵ The high surface areas and crystallinities displayed by these materials have spurred numerous adsorption and diffraction studies.^{38,56} Although some of these have shown the importance of the triangular windows of the cuboctahedral pores in the MOFs as gas storage sites, the presence of additional smaller pores and ligand-based binding sites complicates structural studies. We have recently shown that a family of MOFs based on coordination cages and dabco pillars can be used to glean insight into gas adsorption sites in porous cages.⁵⁷ These frameworks feature cuboctahedral cages connected in three dimensions via dabco molecules. Frameworks of this type, which have been reported for Fe, Co, Cu, and Zn, display BET surface areas in excess of 2000 m²/g. Further, the arrangement of cuboctahedral cages in the MOFs is nearly identical to those found in $M_{24}(t\text{-}Bu\text{-}bdc)_{24}$ cages.

Herein, we report the synthesis and characterization of two novel dabco-pillared metal–organic frameworks based on cobalt and iron cuboctahedral cages. Detailed structural analysis of these solids suggest 5-functionalization of isophthalic acid is sterically limited to methyl substituents. The structures of these MOFs are analogous to a family of *tert*-butyl-functionalized cuboctahedral molecules. We assess the Cr, Mo, and Ru analogues of these cages, in addition to the dabco-pillared MOFs, for high-pressure methane storage. Given the high surface areas and crystallinities of the frameworks, we investigated neutron diffraction as a means to infer the adsorption sites in the molecular solids, which display high volumetric methane uptakes and deliverable capacities. Additionally, we conducted molecular simulations of methane adsorption to confirm the analogous nature of methane binding sites in the materials.

EXPERIMENTAL SECTION

Materials and Methods. With the exception of $Ru_2(OAc)_4Cl$,⁵⁸ metal salts and organic ligands were obtained from commercial sources and used without further purification. For the syntheses of $Co_{24}(Me\text{-}bdc)_{24}(dabco)_6$ and $Ru_{24}(t\text{-}Bu\text{-}bdc)_{24}Cl_{12}$, *N,N*-dimethylformamide (DMF), methanol (MeOH), and chloroform were obtained

from commercial sources and used without further purification. Where syntheses and/or solvent exchanges are performed in a glovebox, solvents were obtained from a solvent drying system and stored in a glovebox on the appropriately sized molecular sieves.

Synthesis of $\text{Co}_{24}(\text{Me-bdc})_{24}(\text{dabco})_6$. In a 100 mL media bottle, $\text{CoCl}_2 \cdot 6\text{H}_2\text{O}$ (2.365 g, 9.941 mmol) and $\text{H}_2\text{Me-bdc}$ (1.801 g, 9.999 mmol) were dissolved in DMF (100 mL) and left to sit at room temperature for 5 days. In a separate 100 mL media bottle, dabco (1.116 g, 9.949 mmol) was dissolved in DMF (100 mL). The resulting cobalt/ligand stock solution (10 mL) was pipetted into five 20 mL glass scintillation vials. The dabco solution (10 mL) was layered onto the cobalt/ligand solution. The resulting solution was capped and heated at 365 K for 12 h. The sample was allowed to cool to room temperature before removing excess solvent. Resulting dark purple cubic crystals were removed from the bottle with fresh DMF and a Pasteur pipet. Solvent exchange was completed by soaking the product in fresh DMF at 383 K for 3 days with the solvent replaced every 12 h. The DMF-washed solid was isolated by removing excess solvent with a Pasteur pipet and then soaked in chloroform at 333 K for 3 days with the solvent replaced every 12 h. Activated material was obtained by evacuation at 348 K.

Synthesis of $\text{Fe}_{24}(\text{Me-bdc})_{24}(\text{dabco})_6$. In a N_2 glovebox, FeCl_2 (0.100 g, 0.789 mmol) and $\text{H}_2\text{Me-bdc}$ (0.142 g, 0.788 mmol) were dissolved in DMF (12 mL) in a capped 20 mL scintillation vial and heated at 393 K for 2 h. Dabco (0.177 g, 1.578 mmol) was then dissolved in acetonitrile (4 mL) and layered on top of the DMF solution. The reaction was allowed to stand for 1 week, after which the reaction mixture was gently swirled and decanted to remove suspended product from larger, higher-density impurities. The light yellow solid was then isolated by centrifugation and soaked in DMF at room temperature for 3 days, replacing the solvent with fresh DMF every 8 h. After DMF washing the solid was washed with benzene by a similar procedure. Over the course of benzene washes, the solid turned a lime-green color. Activated material was obtained by evacuation of frozen benzene at 273 K for 2 days followed by heating under vacuum at 323 K for 2 days. The resulting light green solid is incredibly air sensitive, turning dark brown upon exposure to O_2 .

Synthesis of $\text{M}_{24}(\text{tBu-bdc})_{24}$ Compounds. These compounds were prepared as previously reported.^{40,41,45} However, as surface areas of the Ru^{2+} and Mo^{2+} analogues were not previously reported or were low, respectively, modified solvent exchange and activation procedures were followed. For these, the solids (~200 mg) were soaked in 20 mL of anhydrous, air-free methanol for 48 h, with the solvent replaced by fresh methanol every 8 h. The solids were isolated by vacuum filtration and placed in gas adsorption tubes. The materials were activated under dynamic vacuum with a turbomolecular pump and a heating ramp rate of 0.1 K/min up to their final activation temperatures (Mo = 298 K, Ru = 398 K).

Optimized Synthesis of $\text{Mo}_{24}(\text{tBu-bdc})_{24}$. In an N_2 glovebox, $\text{Mo}_2(\text{OAc})_4$ (0.10 g, 0.234 mmol) and *tert*-butylisophthalic acid (0.052 g, 0.234 mmol) were dissolved in 10 mL of *N,N'*-dimethylpropyleneurea (DMPU) with 5 drops of pyridine and heated at 383 K for 1 day to yield large red crystals. The material was solvent exchanged and activated as reported above.

Gas Adsorption Measurements. Gas adsorption measurements up to 1.1 bar were recorded on a Micromeritics 3Flex gas adsorption analyzer. Surface area measurements were recorded in a liquid nitrogen bath; 298, 308, and 318 K isotherms were recorded in an isothermal bath. Ultra-high-purity gas was used for both the free-space measurements (He) and analyses (N_2 or CH_4). Prior to measurements, samples were considered activated when their outgas rate under static vacuum was ≤ 2 mbar/min. High-pressure isotherms were collected on a Sieverts' apparatus (PCT-Pro-2000 from Hy-Energy Scientific Instruments) using ultra-high-purity gases. Total adsorption was calculated using the National Institute of Standards and Technology Thermochemical Properties of CH_4 and the pore volume of each material, as determined via 77 K N_2 adsorption experiments.

Single-Crystal X-ray Diffraction. Crystals were mounted using viscous oil onto a plastic mesh and cooled to the data collection temperature. Data were collected on a Bruker-AXS APEX II DUO

CCD diffractometer with graphite-monochromated Mo $K\alpha$ radiation ($\lambda = 0.71073 \text{ \AA}$) for $\text{Co}_{24}(\text{Me-bdc})_{24}(\text{dabco})_6$ and with Cu $K\alpha$ radiation ($\lambda = 1.54178 \text{ \AA}$) focused with Goebel mirrors for $\text{Mo}_{24}(\text{tBu-bdc})_{24}$.⁵⁹ Unit cell parameters were obtained from 36 data frames, $0.5^\circ \omega$, from three different sections of the Ewald sphere. The polarized optical properties of the crystal, unit cell parameters, systematic absences, and equivalent reflections in the diffraction data are consistent with $F432$ (209), $F\bar{4}3m$ (216), and $Fm\bar{3}m$ (225) for $\text{Co}_{24}(\text{Me-bdc})_{24}(\text{dabco})_6$ and, uniquely, with $P2_1/n$ (14) for $\text{Mo}_{24}(\text{tBu-bdc})_{24}$. The centrosymmetric space group option for $\text{Co}_{24}(\text{Me-bdc})_{24}(\text{dabco})_6$ yielded chemically reasonable and computationally stable results of refinement. The data were treated with multiscan absorption corrections. The structures were solved using intrinsic phasing methods⁶⁰ and refined with full-matrix, least-squares procedures on F^2 .⁶¹

The cage in $\text{Co}_{24}(\text{Me-bdc})_{24}(\text{dabco})_6$ is located at the intersection of two orthogonal mirror planes and a 3-fold rotoinversion axis. The dabco ligand in $\text{Co}_{24}(\text{Me-bdc})_{24}(\text{dabco})_6$ was treated as an idealized rigid group with rigid bond anisotropic restraints and equal atomic displacement parameters for chemically equivalent atoms. The cage in $\text{Mo}_{24}(\text{tBu-bdc})_{24}$ is located at an inversion center. Although initial solutions for $\text{Mo}_{24}(\text{tBu-bdc})_{24}$ suggested disordered DMPU molecules at the central void as well as between polyhedra, only some of the DMPU molecules coordinated on the outer surface of the cage could be modeled satisfactorily. The *tert*-butyl groups in $\text{Mo}_{24}(\text{tBu-bdc})_{24}$ were restrained such that the quaternary carbon to methyl carbon distance is 1.534(5) \AA , and the methyl carbon to methyl carbon distance is not allowed to be shorter than 2.451(5) \AA . Three *tert*-butyl groups in $\text{Mo}_{24}(\text{tBu-bdc})_{24}$ were given additional idealized geometry with the aromatic carbon to *tert*-butyl carbon distance restrained to 1.527(16) \AA . The atoms in $\text{Mo}_{24}(\text{tBu-bdc})_{24}$ were treated with global three-dimensional anisotropic displacement rigid bond constraints.

The protons on the water molecule at the center of the cage in $\text{Co}_{24}(\text{Me-bdc})_{24}(\text{dabco})_6$ could neither be geometrically calculated nor located and were ignored. All other hydrogen atoms were treated as idealized contributions with geometrically calculated positions and with U_{iso} equal to 1.2 (or 1.5 for methyl) U_{eq} of the attached atom. Remaining electron density that cannot be localized as atoms was treated as a diffused contribution.⁶² The structures have been deposited at the Cambridge Structural Database as CCDC 1881620 and 1891146.

Neutron Diffraction. Experiments were performed on 0.4495 g of $\text{Co}_{24}(\text{Me-bdc})_{24}(\text{dabco})_6$ and 0.7061 g of $\text{Fe}_{24}(\text{Me-bdc})_{24}(\text{dabco})_6$ at the National Institute of Standards and Technology Center for Neutron Research (NCNR). Data were collected at the high-resolution neutron powder diffractometer, BT1, utilizing a Ge(311) monochromator with an in-pile 60' collimator, corresponding to a neutron wavelength of 2.0775 \AA . Activated samples were loaded into vanadium sample cans in a He environment glovebox and sealed with an indium O-ring onto a copper heating block containing a valved outlet for gas loading. After mounting samples onto a bottom-loaded closed cycle refrigerator, samples were cooled to base temperature for measurement. For CD_4 gas doses, the sample was connected to a fixed-volume gas manifold, heated to $T = 120 \text{ K}$, and cooled back to base temperature for measurement. Each of the two samples was dosed with ~0.5 and ~1.5 CD_4 per M, per formula unit. Adsorption was verified barometrically prior to cooling to avoid condensation of the vapor phase for each gas dosage, with each sample dosed twice with CD_4 .

Neutron powder diffraction data were analyzed using Topas Academic.⁶³ The space group $Fm\bar{3}m$ was chosen based on analogous previously reported structures.^{57,64} Initial Pawley refinements were first conducted to determine a background function, lattice parameters, and peak shapes.⁶⁵ The position and orientation of molecules were then solved using rigid bodies with the global optimization method of simulated annealing (SA) in real space.⁶⁶

Rigid bodies were refined similarly to our previous work, using a full methyl-isophthalic acid (Me-bdc) centered and refined on a 96k (x, x, z) position (with two orientations of the methyl group) and a full dabco molecule allowed to rotate along a 48i ($x, 0.5, -x$) position.

Using trigonometric constraints, both only required one variable for rotational movement. As before, activated materials required an additional Me-bdc molecule, as well as a DMF molecule, refined on a 96k (x, x, z) and a 32f (x, x, x) site, respectively, with the additional Me-bdc allowed to freely move and the DMF molecule to rotate around a fixed axis using one degree of freedom. The refined positions of these two molecules represent their disordered, occupied space, rather than absolute positions. Once a reasonable solution was found, the number of atoms and their Wyckoff positions were corrected, followed by refining occupancies and thermal parameters separately. Additionally, occupancies that refined within error of unity were fixed and thermal parameters were fixed across each rigid body.

Once activated structures were determined, SA refinements were conducted on CD_4 gas loaded data. Initial positions were determined using Fourier difference maps in both Topas Academic and GSAS.^{63,67} This involved the addition of four CD_4 molecules: one at the open metal site on a 48i ($x, x, 0.5$) position, one in the corners of triangular windows on a 96k (x, x, z) site, one in the corners of square windows on a 96j ($0, y, z$) site, and one between four triangular windows on a 32f (x, x, x) site. Initially the orientation of each molecule was fixed according to known methane interactions,^{68,69} which additionally mapped each CD_4 molecule onto itself. Each molecule was then allowed to freely rotate, while keeping as many variables fixed as possible, then additionally allowed to refine off each Wyckoff position, all while adjusting occupancies as needed. Final CD_4 positions/orientations were chosen based on how each additional freedom of movement improved the refinement. Where possible, the activated structure was fixed throughout this process. Once final CD_4 positions were obtained, occupancies, thermal parameters, and lattice parameters were refined.

The resulting refinements from this process are shown in Figures S1–S6. Despite numerous attempts at deuteration on these compounds, dabco molecules contained 10–25% hydrogen and Me-bdc molecules contained 65–85% hydrogen. Given that complete removal of excess DMF and Me-bdc was not possible without structural degradation, there is considerable incoherent scattering due to hydrogen. However, Weller et al.,^{70,71} as well as our previous MOF work,⁷² have shown that neutron powder diffraction is quite possible with various amounts of hydrogen in crystalline materials, with hydrogen positions readily accessible due to their negative contrast. It is understandable that due to the amount of hydrogen, as well as the large unit cell, the patterns do not contain much information beyond $Q = 2 \text{ \AA}^{-1}$, despite containing sharp crystalline peaks. The Rietveld analysis indicates that there is a good agreement between the data and the models (Figures S1 and S2), with the resulting activated materials being commensurate with previously reported analogous materials. The model CD_4 -dosed structures are additionally in exceptional agreement with the neutron data (Figures S3–S6).

Computational Methodology. We used our open-source software for classical molecular modeling in nanoporous crystals, PorousMaterials.jl. The Julia code and input files to reproduce our calculations are available on Github.⁷³

Molecular Model. We approximate the material as crystalline and rigid, using the experimentally determined crystal structures (with disorder repaired to arrive at chemically valid structures) as input to our molecular simulations. We model the potential energy of a microstate of gas molecules in the material as pairwise additive interatomic interactions described by 12–6 Lennard-Jones potentials. We model a methane molecule as a single, “united-atom” interaction site with parameters taken from the Transferable Potentials for Phase Equilibria (TraPPE) force field;⁷⁴ molecular simulations using these parameters accurately reproduce the normal boiling point and critical properties of methane. For the atoms composing the materials, we take Lennard-Jones parameters for C, H, N, and O from the Dreiding force field⁷⁵ and for Co and Mo from the Universal Force Field⁷⁶ since they are missing from DREIDING. The nonbonded DREIDING force field parameters were tuned to reproduce crystal structures and sublimation energies of a large set of compounds. Parameters for cross-atomic-species interactions follow from the Lorentz–Berthelot mixing rules. We truncate the Lennard-Jones

potentials at a cutoff distance of 14 Å and apply periodic boundary conditions to the simulation box consisting of a supercell of the crystal (box in Figure 6).

Level Surfaces of the Potential Energy. To generate the visualizations in Figure 6 of the level surfaces of the potential energy $V = V(x)$ of an isolated methane molecule at position x in the crystal, we first superimpose on the supercell a regular grid of points with less than 0.1 Å grid spacing. Then, we compute the potential energy of a methane molecule at each grid point and store it in a 3D array. We visualize the level surfaces of $V(x)$, represented as a .cube file, using the VisIt visualization tool.⁷⁷

Molecular Simulations of Methane Adsorption. We obtained the simulated methane adsorption isotherms at 298 K in Figure S88 by conducting a set of Markov chain Monte Carlo simulations of the grand-canonical (μVT) statistical mechanical ensemble⁷⁸ at different chemical potentials. The simulation volume V is a supercell of the crystal. We relate the bulk gas pressure to a corresponding chemical potential using the Peng–Robinson equation of state for methane. As Markov chain transitions, we propose particle insertions, deletions, translations, and reinsertions with probability 0.35, 0.35, 0.25, and 0.05, respectively. A proposal to transition to a new microstate is accepted with probabilities governed by the Metropolis–Hastings rules so as to sample the grand-canonical statistical ensemble. Initiating the system with zero adsorbed molecules, we conducted 100 000 Monte Carlo burn-in cycles, then 100 000 Monte Carlo production cycles during which we collected statistics to compute, for example, the average number of adsorbed gas molecules in the system. A Monte Carlo cycle is defined as $\max(20, n)$ Markov chain transition proposals, where n is the number of molecules in the system immediately before a new cycle begins. Figures S88 and S89 compare the simulated and experimental methane adsorption isotherms and heats of adsorption; the simulations overestimate adsorption, but agreement with the heats of adsorption is good.

Methane Spatial Probability Density. We characterized the spatial probability density of methane molecules in the material during our grand-canonical Monte Carlo simulations as follows. First, we partition the simulation box (the supercell of the crystal) into a regular grid of voxels whose centers are less than 0.5 Å apart. Then, during the simulation, at the end of each Monte Carlo production cycle, we effectively count the number of methane molecules that belong to each voxel (“take a snapshot”). At the end of the simulation, we have a 3D histogram (normalized by the number of snapshots) of the positions of the methane molecules observed during the simulation. This gives an approximation to the integral of the spatial probability density of methane over the voxel. We visualize the spatial probability density, represented as a .cube file, using the VisIt visualization tool. We use the same scale to determine color for each pressure so the visualized densities can be readily compared across pressures. We used 100 000 burn-in cycles and 200 000 production cycles—thus, taking 200 000 snapshots of methane molecules—to generate the probability density plots for methane adsorption simulations at 1, 5, 35, and 65 bar of pressure.

RESULTS AND DISCUSSION

Although metal–organic framework surface areas can often be optimized regardless of the exact nature of the synthesis, solvent exchange, and activation procedures, we have recently shown that these factors are vitally important for realizing maximal surface area in coordination cages.⁶⁹ The lack of three-dimensional connectivity in molecular systems often results in significant structural rearrangement upon solvent exchange and evacuation. Cages can also display differing porosity depending on the space group into which they crystallize. For one of the coordination cages displaying high surface area, $\text{Cr}_{24}(\text{tBu-bdc})_{24}$, the solid undergoes two phase changes upon activation, from $P4_2/mmm$ to $C2$ to $C2/c$. In spite of this, the solid displays both high surface area and thermal stability. Encouraged by this, we sought to

reinvestigate the reported $M_{24}(\text{tBu-bdc})_{24}$ ($M = \text{Cu}^{2+}$, Mo^{2+} , $\text{Ru}^{2+/3+}$) family of cages. For these adsorbents, surface areas are either entirely lacking (Ru) or reported to be significantly lower than the chromium(II)-based material ($\text{Cu} = \sim 225 \text{ m}^2/\text{g}$, $\text{Cr} = 1135 \text{ m}^2/\text{g}$, $\text{Mo} = 437 \text{ m}^2/\text{g}$).⁷⁹

Regardless of synthesis, solvent exchange, or activation conditions, we were unable to improve upon the surface area of $\text{Cu}_{24}(\text{tBu-bdc})_{24}$. This was similarly the case for $\text{Cu}_{12}(\text{cdc})_{12}$ ($\text{cdc}^{2-} = \text{carbazoledicarboxylate}$), an octahedral coordination cage that displayed significantly diminished surface areas as compared to its chromium(II) and molybdenum(II) counterparts.⁶⁹ $\text{Ru}_{24}(\text{tBu-bdc})_{24}\text{Cl}_{12}$ displayed a comparable surface area to $\text{Cr}_{24}(\text{tBu-bdc})_{24}$ by utilizing specific solvent exchange and activation methods. To achieve this, as-synthesized solid was thoroughly exchanged with anhydrous, air-free methanol. Upon activation at 348 K, the solid displays a BET (Langmuir) surface area of 1057 (1540) m^2/g (Figure 2). This value is in

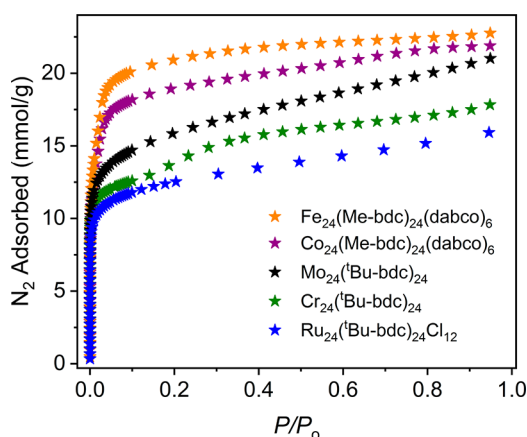


Figure 2. N_2 adsorption isotherms collected at 77 K for the three $M_{24}L_{24}$ cages and two analogous pillared cage-based metal–organic frameworks.

relatively good agreement with the value expected based on change in formula unit mass as compared to the Cr^{2+} cage (962 m^2/g BET, 1522 m^2/g Langmuir). The infrared spectrum of the activated material indicates the absence of metal- or pore-bound DMF or methanol, confirming complete desolvation of the cage (Figure S19). Despite demonstrating good porosity, powder X-ray diffraction reveals major structural rearrangement to the point of amorphization upon solvent evacuation (Figure S20), suggesting the cuboctahedra cages are rotationally disordered relative to one another.

In order to optimize the surface area of $\text{Mo}_{24}(\text{tBu-bdc})_{24}$, a significantly altered strategy was employed. Solvent exchange and activation of a sample that was prepared via the previously reported route (1,2-dichlorobenzene/pyridine mixture) afforded surface areas consistently below 800 m^2/g .⁷⁹ For $\text{Mo}_{12}(\text{cdc})_{12}$ we previously showed that surface area is significantly affected by synthetic conditions, with higher symmetry space groups affording higher surface area materials.⁶⁹ Although varying synthetic conditions, including solvent, cosolvent, acid addition, and reaction temperature typically afforded a cage that crystallized in the same space group as the previously reported solid, $I4/m$, utilization of a pyridine/DMPU mixture for the synthesis afforded an optimally porous material that crystallized in $P2_1/n$. Interestingly, the cage synthesized via this route adopts the same cuboctahedral structure arranged in the same orientation as the

reported structure but displays a significantly increased surface area. Here, after room-temperature methanol exchanges and activation, $\text{Mo}_{24}(\text{tBu-bdc})_{24}$ is shown to have a BET (Langmuir) surface area of 1321 (2105) m^2/g . This value is significantly higher than the value predicted based on the increased formula mass of the cage as compared to $\text{Cr}_{24}(\text{tBu-bdc})_{24}$ (BET = 977 m^2/g) and, to the best of our knowledge, represents a new record value for porous coordination cages.

Close investigation of the crystal structures of all three porous $M_{24}(\text{tBu-bdc})_{24}$ materials reveals multiple possible structural factors contributing to their high porosity (Figures S21–S40). The structures contain solvent–solvent interactions between metal-bound solvent molecules on adjacent cages. Given the ease at which solvent is removed from Cr^{2+} , Mo^{2+} , and $\text{Ru}^{2+/3+}$ paddlewheels, and as confirmed via infrared spectroscopy, these interactions are likely no longer present in the activated phases of these solids. It has been previously posited that paddlewheel–paddlewheel interactions account for their high surface areas and stabilities.⁴³ These types of interactions are relatively common with acetic acid-based paddlewheels. Here, the axial site of the paddlewheel cation coordinates to a carboxylate oxygen on an adjacent paddlewheel. This interaction is propagated throughout the structure to essentially form one-dimensional chains. However, examples of this are relatively rare for Cr^{2+} and Mo^{2+} paddlewheels.⁸⁰ Further, the necessity of a charge-balancing anion in $\text{Ru}^{2+/3+}$ structures prevents this interaction. The cage–cage interactions that are most likely predominantly involved are the van der Waals contacts between *tert*-butyl groups on adjacent molecules. Here, each *tert*-butyl group interacts with two groups from neighboring cages. The body-centered cubic packing arrangement of cuboctahedra facilitates this interaction. As a result, all 24 *tert*-butyl groups on each cage feature these interactions. In all three structures, the average distance between adjacent methyl groups on *tert*-butyl functionalities is $\sim 4.0 \text{ \AA}$. This value is consistent with the van der Waals radius of a methyl group of 2.0 Å . Ultimately, rather than solvent–solvent interactions or paddlewheel–paddlewheel interactions, it is the large number of ligand–ligand interactions that endow the solids with sufficient thermal stabilities to survive solvent removal/activation.

In order to better understand surface areas of *tert*-butyl-functionalized cuboctahedral cages, it is useful to compare them to the previously reported dabco-pillared MOFs, the structures of which are highly similar. For these, cuboctahedral cages are similarly arranged in a body-centered-cubic arrangement (Figure 3). Dabco molecules coordinated to the exterior sites of the cages connect them in three dimensions. Analogous to the structures of the molecular materials, the 5-position of the ligands of three cages are pointed to the same position. However, in the MOF the ligands are in much closer proximity. This is a result of the dabco pillar bringing the cages in closer contact as compared to the molecular case. The paddlewheel–paddlewheel distance in the pillared MOF is approximately 6.75 Å , whereas this is expanded to 7.42 Å for the cages. This again points to the importance of ligand functionalization in designing and synthesizing these metal–organic cages. Close inspection of $M_{24}(\text{bdc})_{24}(\text{dabco})_6$ ($M = \text{Fe}$, Co , Cu , Zn) suggests the structure will be incompatible with large functional groups. In order to interrogate this, we turned to the synthesis of new members of the $M_{24}(\text{R-bdc})_{24}(\text{dabco})_6$ family with various metal cations and ligand functional groups.

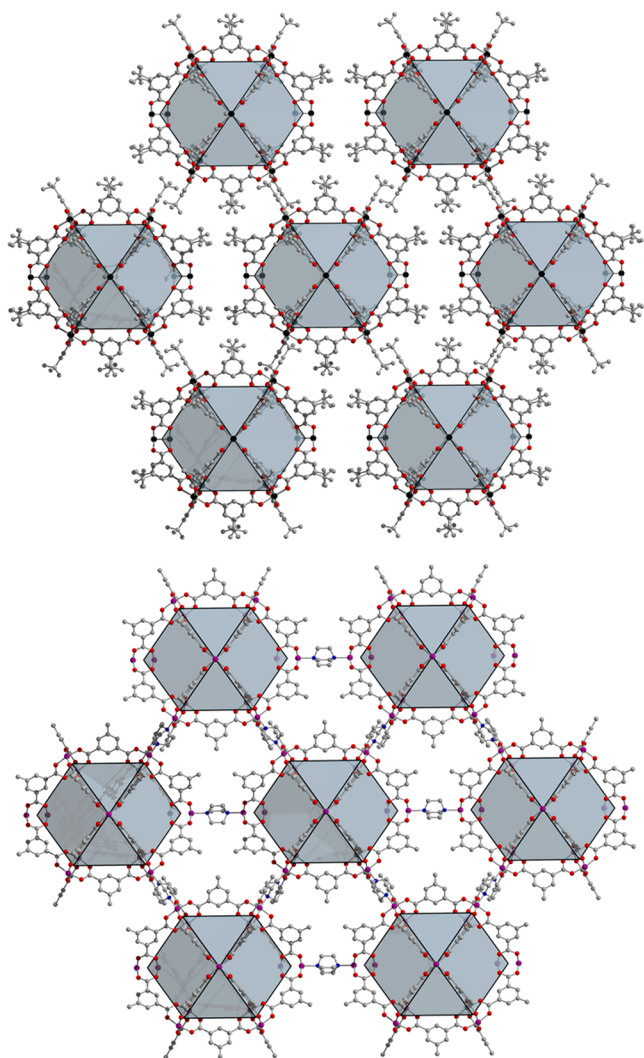


Figure 3. Structures of $\text{Mo}_{24}(\text{}^t\text{Bu-bdc})_{24}$ (top) and $\text{Co}_{24}(\text{Me-bdc})_{24}(\text{dabco})_6$ (bottom) illustrating the similarities between the cage and MOF structures, respectively. In the former, van der Waals contacts between *tert*-butyl groups give rise to three-dimensional pseudoconnectivity, whereas in the latter, metal-coordinated dabco ligands pillar the cages into three dimensions. Black, purple, red, gray, and blue atoms represent Mo^{2+} , Co^{2+} , O, C, and N, respectively. Solvent molecules and hydrogen atoms have been omitted.

Although $\text{Cu}_{24}(\text{OH-bdc})_{24}(\text{dabco})_6$ can be isolated via the addition of dabco to a solution of presynthesized cage, these materials are typically prepared via a one-pot solvothermal reaction, as the cages that comprise them are neither soluble nor synthetically accessible. The typically soluble Cr^{2+} - and Mo^{2+} -based cages lack the metal acidity to strongly coordinate dabco, a result of the presence of M–M quadruple bonds for these cations. To prepare new pillared cages, we screened the reaction of various Mn, Fe, Co, Ni, Cu, Zn, and Mo salts with R-bdc (R = methyl, alkoxides, *tert*-butyl, hydroxy, amino, cyano, nitro, and bromo) in the presence of dabco in various amide-based solvent systems. Consistent with the lack of pore space for bulky functional groups, we were able to isolate crystalline product only for $\text{M}_{24}(\text{Me-bdc})_{24}(\text{dabco})_6$ (M = Fe, Co, Cu) and $\text{Fe}_{24}(\text{OH-bdc})_{24}(\text{dabco})_6$, as confirmed by powder X-ray and neutron diffraction. Of these, only $\text{M}_{24}(\text{Me-bdc})_{24}(\text{dabco})_6$ (M = Fe, Co) displayed high levels of porosity, even after precise activation conditions, with BET

(Langmuir) surface areas of 1937 (2264) and 1727 (2252) m^2/g for the iron and cobalt analogues, respectively. These numbers essentially represent the upper limits of surface areas for analogous cage materials, as in the pillared MOFs both the interior and exterior surfaces of the cages are potentially accessible to probe molecules. Porous or potentially porous cages that lack directional ligand functional groups that can interact tend to close pack, exemplified by the low surface area of $\text{Cu}_{24}(\text{bdc})_{24}$.³⁹ When all of the pore windows are blocked off, the solids are inaccessible to nitrogen or carbon dioxide. Often these materials display low levels of porosity, as only the interior surface of the cages are nitrogen accessible. However, this should be highly tunable based on judicious ligand functionalization.

Given the nearly isostructural nature of the *tert*-butyl-based porous cages and the dabco-pillared MOFs (Figure 3), the latter offer a unique and powerful opportunity to further understand the former in terms of the storage of small molecules. At 298 K, all five materials display similar methane uptake up to one bar, ranging from 0.4 to 0.7 mmol/g (Figures S67–S72). At low pressures and correspondingly low uptake values, the one bar gravimetric capacities do not trend with BET or Langmuir surface areas. Temperature dependence of adsorption indicates adsorption enthalpies ranging from -15 to -21 kJ/mol and following the trend $\text{Ru} < \text{Mo} < \text{Cr} < \text{Fe} < \text{Co}$. This range of adsorption enthalpies is well within the range of values typically seen for porous solids.⁸¹ Methane adsorption enthalpies in the two MOFs are lower, as their metal cations, which have been shown to be highly polarizing adsorption sites, are blocked on the exterior surface with pillaring dabco and on the interior surface with DMF. This effectively lowers the average adsorption enthalpy of the materials.

To further evaluate the methane storage properties of all five materials, high-pressure adsorption isotherms were collected at 298 K (Figures S74–S85). At both 35 and 65 bar, the total gravimetric capacities generally correlate with BET surface areas with the uptake values following the trend $\text{Ru} \sim \text{Cr} < \text{Mo} < \text{Fe} < \text{Co}$. The gravimetric capacities, which range from 138 to 216 cm^3/g , are generally comparable to many MOFs with similar surface areas.⁸¹ Given the greatly varying crystallographic densities of the solids, the volumetric uptakes of the solids are significantly altered with Cr ($88 \text{ cm}^3(\text{STP})/\text{cm}^3$) $<$ $\text{Ru} \sim \text{Mo} < \text{Fe} < \text{Co}$ ($144 \text{ cm}^3(\text{STP})/\text{cm}^3$) (Figure 4). In terms of the porous cages, the gravimetric uptakes of these three materials at 35 and 65 bar are actually lower than expected based on their surface areas and as compared to our previously reported $\text{M}_{12}(\text{cdc})_{12}$ cages (M = Cr^{2+} , Cu^{2+} , Mo^{2+} ; cdc^{2-} = carbazoledicarboxylate). This is accentuated when comparing their volumetric capacities. For example, $\text{Mo}_{12}(\text{cdc})_{12}$ displays 298 K volumetric capacities of 111.5 and 150.0 $\text{cm}^3(\text{STP})/\text{cm}^3$ at 35 and 65 bar, respectively. Under these same conditions, $\text{Mo}_{24}(\text{}^t\text{Bu-bdc})_{24}$ shows uptakes of 97 and 120 $\text{cm}^3(\text{STP})/\text{cm}^3$, despite having a BET surface area that is 20% higher than the carbazole-based cage. This discrepancy is likely a result of the absence of highly favorable CH_4 binding sites in $\text{Mo}_{24}(\text{}^t\text{Bu-bdc})_{24}$.

As methane storage materials, deliverable capacity, cyclability, and adsorption/desorption kinetics are important considerations. As shown in Figure 5, two representative adsorbents, $\text{Cr}_{24}(\text{}^t\text{Bu-bdc})_{24}$ and $\text{Co}_{24}(\text{Me-bdc})_{24}(\text{dabco})_6$, display no loss in capacity at 298 K over 10 adsorption/desorption cycles. Under these conditions, the kinetics of both ad/desorption are

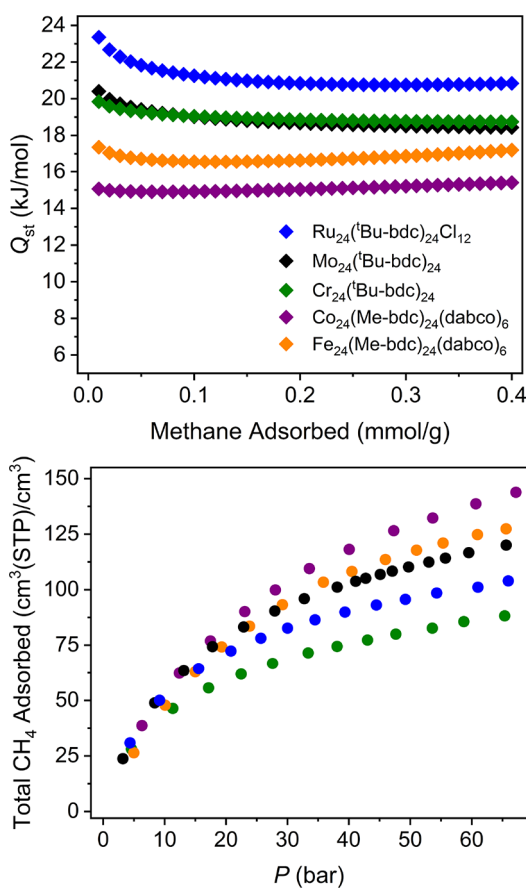


Figure 4. (Top) Isothermic heats of CH₄ adsorption calculated from fits to variable-temperature low-pressure uptake experiments. (Bottom) High-pressure total methane adsorption in M₂₄(^tBu-bdc)₂₄ (black = Mo, blue = Ru, green = Cr) and M₂₄(Me-bdc)₂₄(dabco)₆ (orange = iron, purple = cobalt) at 298 K.

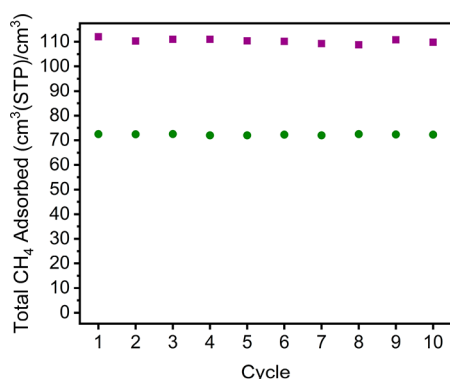


Figure 5. Methane cycling in Cr₂₄(^tBu-bdc)₂₄ (green circles) and Co₂₄(Me-bdc)₂₄(dabco)₆ (purple squares) at 298 K and a final adsorption pressure of 35 bar. Between cycles, the samples were reactivated under dynamic vacuum for 5 min.

very rapid, with 35 bar adsorption equilibria achieved in under 2 min. Desorption was carried out by placing the materials under dynamic vacuum at 298 K for 5 min. For a pressure swing from 35 to 5.8 bar, deliverable capacities of all five solids range from 45 (Cr) to 80 (Co) cm³(STP)/cm³. Increasing the adsorption uptake pressure to 65 bar increases the deliverable capacities to up to 102 cm³(STP)/cm³ (deliverable capacities for these materials and comparable MOFs are listed in Tables S8 and S9). Although these fall short of the record values of

the best performing metal–organic frameworks (up to 200 cm³(STP)/cm³),¹⁷ they are nearly on par when taking actual bulk density (rather than crystallographic density) into consideration. With this in mind, both Mo₂₄(^tBu-bdc)₂₄ and Co₂₄(Me-bdc)₂₄(dabco)₆ have 65–5.8 bar working capacities of 72 cm³(STP)/cm³ as compared to 83 cm³(STP)/cm³ for HKUST-1.⁸¹ The molecular nature of the cages reported here may offer an advantage in this regard, as their solubility may afford a means to tune phase and thus bulk density.

We next conducted molecular simulations of methane adsorption in both Co₂₄(Me-bdc)₂₄(dabco)₆ and Mo₂₄(^tBu-bdc)₂₄. Our aims were to (i) elucidate the methane adsorption sites in the structures and the sequence in which they are occupied as pressure increases and (ii) juxtapose the hierarchy of adsorption sites in these two structures that harbor isostructural cuboctahedral cages. To characterize the spatial probability density of methane, we first partitioned the simulation box into a regular grid of voxels. Then, we took snapshots during grand-canonical Monte Carlo simulations of methane adsorption and counted the methane molecules that belonged to each voxel. Figure 6a–d visualize the spatial probability density of methane in Mo₂₄(^tBu-bdc)₂₄ at 298 K and 1, 5, 35, and 65 bar. At low pressures, methane adsorbs primarily at the center of the triangular window. At higher pressures, the corners of the triangular windows and square windows are populated. Figure 6e shows level surfaces of the computed potential energy of a methane molecule in the cage, confirming that the strongest binding sites are offered by the triangular window, followed by the corners of the square windows. The spatial probability density of methane in Co₂₄(Me-bdc)₂₄(dabco)₆ (Figure S86) shows a similar trend, where the triangular windows are filled first, then the corners of the square windows.

To confirm the mechanism of CH₄ binding in these materials, we turned to neutron powder diffraction. The lack of long-range order and low crystallinity in porous cages often preclude the use of diffraction methods for in-depth characterization. Given the structural similarities of the cages and frameworks, diffraction experiments on the porous frameworks can be used to infer information about adsorption sites, as our computational modeling confirms the similar nature of the adsorption sites between the framework and cage materials. Detailed powder neutron diffraction experiments performed on Fe₂₄(Me-bdc)₂₄(dabco)₆ and Co₂₄(Me-bdc)₂₄(dabco)₆ allowed us to precisely determine CD₄ binding sites and occupancies. For both frameworks, methane doses of 0.5/M²⁺ and 1.5 CD₄/M²⁺ were utilized. In Fe₂₄(Me-bdc)₂₄(dabco)₆ this corresponds to adsorption uptakes (pressures) of 36.8 cm³/g (4.2 bar) and 110.0 cm³/g (17.9 bar). As Co₂₄(Me-bdc)₂₄(dabco)₆ exhibits similar methane uptakes and a similar molar mass, the loadings correspond to 36.5 cm³/g (3.5 bar) and 109.4 cm³/g (16 bar).

In both materials at both loadings, four different methane binding sites are apparent (Table 1), three of which show loading-dependent occupancies (Figures S90–S101). The highest occupancy site in both frameworks is the center of the six triangular windows in the cage (Figure 7). Methane adsorbs in the bowl that is formed by three paddlewheel sites and three Me-bdc ligands. The CD₄–arene distances for the iron and cobalt frameworks are 4.12(7) and 4.15(4) Å, respectively. Together with the methyl groups of the ligand, this center site forms the basis for additional adsorption sites at the triangular window that is disordered over three positions.

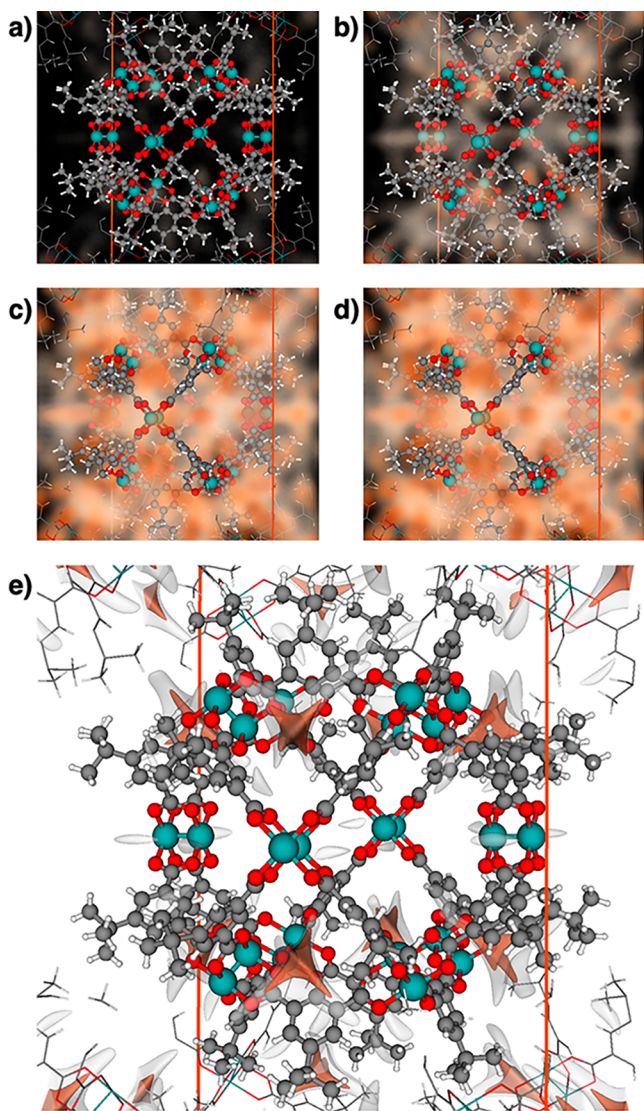


Figure 6. Binding site elucidation via molecular modeling and simulation. Visualization of the spatial probability density of methane in $\text{Mo}_{24}(\text{tBu-bdc})_{24}$ during grand-canonical Monte Carlo simulations at 298 K and 1 bar (a), 5 bar (b), 35 bar (c), and 65 bar (d). Methane primarily adsorbs in the center of the triangular window at low pressure. At higher pressures, the corners of the triangular and square windows become populated. (e) Level surfaces of the potential energy of a methane molecule in the cage at -16 kJ/mol (orange) and -14 kJ/mol (white) highlight the triangular window and four corners of the square window as the most favorable binding sites.

Table 1. Methane Occupancies in $\text{M}_{24}(\text{Me-bdc})_{24}(\text{dabco})_6$ ($\text{M} = \text{Fe}, \text{Co}$) at Various Loadings

site	0.5 $\text{CD}_4/\text{Fe}^{2+}$	1.5 $\text{CD}_4/\text{Fe}^{2+}$	0.5 $\text{CD}_4/\text{Co}^{2+}$	1.5 $\text{CD}_4/\text{Co}^{2+}$
center of triangle	0.51(4)	0.62(4)	0.59(2)	0.62(2)
metal	0.28(2)	0.29(2)	0.21(2)	0.21(1)
top of triangle	0.20(2)	0.77(2)	0.14(2)	0.92(1)
corner of square	0.13(1)	0.66(2)	0.13(1)	0.69(1)

These sites involve $\text{CD}_4\text{-CD}_4$ distances of ~ 3.6 Å and $\text{CD}_4\text{-methyl}$ distances of approximately 4 Å. It is of interest to note that the pillaring dabco ligands are adjacent to this site and within van der Waals contact of the CD_4 molecule. As a result, dabco displays less rotational disorder as compared to the bare

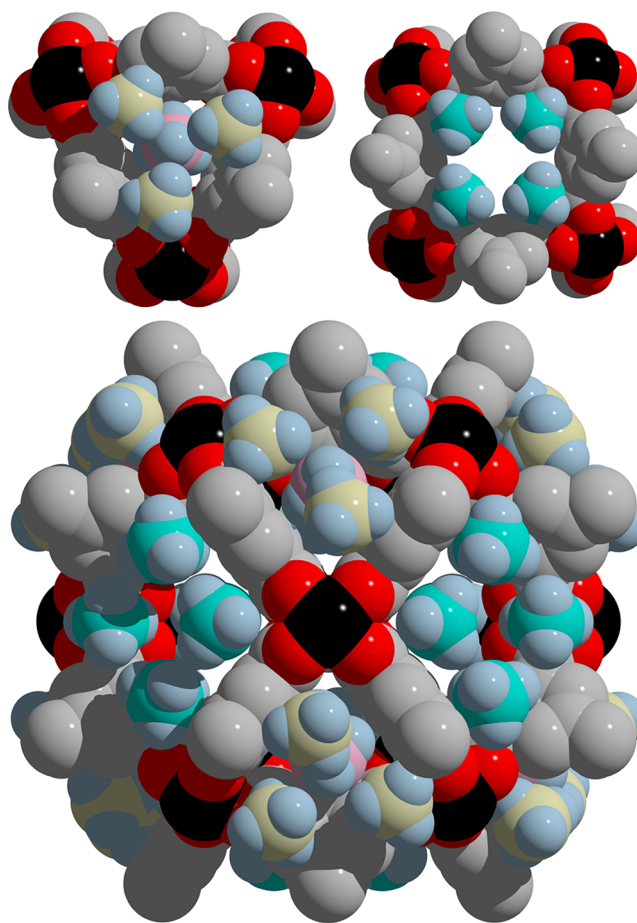


Figure 7. Methane binding sites in $\text{Co}_{24}(\text{Me-bdc})_{24}(\text{dabco})_6$ as determined by powder neutron diffraction. At loadings up to 1.5 $\text{CD}_4/\text{M}^{2+}$, four binding sites are apparent: the center of the triangular window, corners of the triangular window, corners of the square window, and open metal coordination sites on the interior surface of the cage. Black, red, gray, and blue spheres represent cobalt, oxygen, carbon, and deuterium, respectively. The pink, yellow, and teal spheres represent carbon atoms of adsorbed methane.

structures. The metal site on the interior surface of the cuboctahedron is the second highest occupancy site in both materials (~ 0.28 and 0.21 for Fe and Co, respectively). The occupancy of this site, with an M-C distance of approximately 2.3 Å, is loading independent. This is likely a result of the presence of metal-coordinated DMF and unreacted ligand on the interior surface of the cage, which was also observed in the IR spectra of the material. The corners of the square windows of the cuboctahedral cages serve as the final binding sites at these loadings. At this site methane is interacting with the carboxylate group of the ligand with $\text{CD}_4\text{-C}$ distances of ~ 3.4 Å. These binding sites have also been observed in the cuboctahedral pore of HKUST-1 with similar ligand- CD_4 and $\text{CD}_4\text{-CD}_4$ distances (Figures S102, S103).⁶⁸ Between the six square windows and eight octahedral windows in the cuboctahedron, these account for 56 adsorption sites. Full population of these adsorption sites would afford gravimetric uptake capacities of 192, 165, and 154 cm^3/g for $\text{Cr}_{24}(\text{tBu-bdc})_{24}$, $\text{Mo}_{24}(\text{tBu-bdc})_{24}$, and $\text{Ru}_{24}(\text{tBu-bdc})_{24}\text{Cl}_{12}$, respectively. On average, the cages achieve 90% of these uptake values at 65 bar. Previous studies at higher methane loadings in

HKUST-1 indicate additional methane binding sites on the interior surface of the cuboctahedral cage.⁶⁸

The higher-loading powder neutron diffraction data shed light on the large discrepancy between the gravimetric and volumetric uptakes of $M_{24}(\text{tBu-bdc})_{24}$ and $M_{12}(\text{cdc})_{12}$ materials. At a pressure of approximately 30 bar, the entire center of the cuboctahedral cage remains essentially empty, whereas the corresponding octahedral, carbazole-based cage displays negligible wasted volume. Further, the 12-metal carbazole cages display minimal extracage pore volume. Comparison of pore size distribution plots for both cages reveals the presence of significant pore size greater than 15 Å for the cuboctahedral cage. In terms of volumetric gas storage, this wasted pore space is detrimental to the overall deliverable capacity of an adsorbent. However, the molecular nature of these cages can be utilized in this regard by judicious ligand functionalization to tune the extracage pore space. Further, their solubility and propensity to crystallize into a number of space groups and crystal morphologies render them completely tunable for small-molecule storage applications.

CONCLUSIONS

By optimizing synthesis, solvent exchange, and activation conditions, surface areas of porous coordination cages can approach those displayed by three-dimensional metal–organic frameworks. We have shown this to be the case for a family of *tert*-butyl-functionalized cuboctahedral coordination cages. The Cr^{2+} , Mo^{2+} , and $\text{Ru}^{2+/3+}$ analogues of these molecules display high BET surface areas, with $\text{Mo}_{24}(\text{tBu-bdc})_{24}$ having a porous coordination cage record surface area of 1320 m²/g. Additionally, calculations demonstrated molecular gas interactions are analogous in nature to pillared cuboctahedra coordination cages. Although the methane storage properties of these materials are not remarkable when compared to flexible or ultrahigh surface area metal–organic frameworks, the fact that they are molecular renders them significantly more tunable than their MOF counterparts. Further, in terms of deliverable capacities based on bulk as opposed to crystallographic densities, $\text{Mo}_{24}(\text{tBu-bdc})_{24}$ boasts 87% the methane capacity of HKUST-1, despite having a surface area that is approximately 40% lower. Moving forward, this insight will aid in the development of future porous metal–organic materials. In particular, by precisely tuning both the pore size and shape of the cage, in addition to the pore space between cages, adsorbents with true molecular-level control are attainable.

ASSOCIATED CONTENT

Supporting Information

The Supporting Information is available free of charge on the ACS Publications website at DOI: 10.1021/jacs.9b05872.

Synthetic details, neutron diffraction fits, gas adsorption plots (PDF)

Crystal structure data (CIF)

AUTHOR INFORMATION

Corresponding Author

*edb@udel.edu

ORCID

Cory M. Simon: 0000-0002-8181-9178

Eric D. Bloch: 0000-0003-4507-6247

Author Contributions

^{||}G.R.L. and E.J.G. contributed equally.

Funding

We are grateful to the University of Delaware for start-up funds. The manuscript was prepared under cooperative agreement #70NANB17H302 from NIST, U.S. Department of Commerce. We acknowledge the support of the National Institute of Standards and Technology, U.S. Department of Commerce, in providing the neutron research facilities used in this work. This work utilized facilities supported in part by the National Science Foundation under Agreement No. DMR-0944772. B.A.T. recognizes the National Academies/National Research Council for his Postdoctoral Fellowship. This research used resources of the Advanced Photon Source, a U.S. Department of Energy (DOE) Office of Science User Facility operated for the DOE Office of Science by Argonne National Laboratory under Contract No. DE-AC02-06CH11357. We thank the staff of 17-BM for help with synchrotron data collection. A portion of this work was supported by the National Institutes of Health under award number P20GM104316. The content is solely the responsibility of the authors and does not necessarily represent the official views of the National Institutes of Health. We thank the ACS Petroleum Research Fund for support of C.A.R.

Notes

The authors declare no competing financial interest.

ACKNOWLEDGMENTS

We thank Maxwell I. Martin for assistance with crystal structure data acquisition/evaluation.

REFERENCES

- (1) Keum, Y.; Park, S. P.; Chen, Y.-P.; Park, J. Titanium-Carboxylate Metal-Organic Framework based on an Unprecedented Ti-Oxo Chain Cluster. *Angew. Chem., Int. Ed.* **2018**, *57*, 14852–14856.
- (2) Piscopo, C. G.; Trapani, F.; Polyzoidis, A.; Schwarzer, M.; Pace, A.; Loebbecke, S. Positive Effect of the Fluorine Moiety on the Oxygen Storage Capacity of UiO-66 Metal-Organic Frameworks. *New J. Chem.* **2016**, *40*, 8220–8224.
- (3) Rieth, A. J.; Tulchinsky, Y.; Dinca, M. High and Reversible Ammonia Uptake in Mesoporous Azolate Metal-Organic Frameworks with Open Mn, Co, and Ni Sites. *J. Am. Chem. Soc.* **2016**, *138*, 9401–9404.
- (4) Moreau, F.; Silva, I. D.; Smail, N. H.; Easun, T. L.; Savage, M.; Godfrey, H. G. W.; Parker, S. F.; Manuel, P.; Yang, S.; Schroder, M. Unravelling Exceptional Acetylene and Carbon Dioxide Adsorption Within a Tetra-Amide Functionalized Metal-Organic Framework. *Nat. Commun.* **2017**, *8*, 14085–14094.
- (5) Savage, M.; Cheng, Y.; Easun, T. L.; Eyley, J. E.; Argent, S. P.; Warren, M. R.; Lewis, W.; Murray, C.; Tang, C. C.; Frogley, M. D.; Clinque, G.; Sun, J.; Rudic, S.; Murden, R. T.; Benham, M. J.; Fitch, A. N.; Blake, A. J.; Ramirez-Cuesta, A. J.; Yang, S.; Schroder, M. Selective Adsorption of Sulfur Dioxide in a Robust Metal-Organic Framework Material. *Adv. Mater.* **2016**, *28*, 8705–8711.
- (6) Barea, E.; Montoro, C.; Navarro, J. A. R. Toxic Gas Removal - Metal-Organic Frameworks for the Capture and Degradation of Toxic Gases and Vapours. *Chem. Soc. Rev.* **2014**, *43*, 5419–5430.

- (7) Liao, Y.; Zhang, L.; Weston, M. H.; Morris, W.; Hupp, J. T.; Farha, O. K. Tuning Ethylene Gas Adsorption via Metal Node Modulation: Cu-MOF-74 for a High Ethylene Deliverable Capacity. *Chem. Commun.* **2017**, *53*, 9376–9379.
- (8) Britt, D.; Tranchemontagne, D.; Yaghi, O. M. Metal-Organic Frameworks with High Capacity and Selectivity for Harmful Gases. *Proc. Natl. Acad. Sci. U. S. A.* **2008**, *105*, 11623–11627.
- (9) Zhang, H.; Deria, P.; Farha, O. K.; Hupp, J. T.; Snurr, R. Q. A Thermodynamic Tank Model for Studying the Effect of Higher Hydrocarbons on Natural Gas Storage on Metal-Organic Frameworks. *Energy Environ. Sci.* **2015**, *8*, 1501–1510.
- (10) Pham, T.; Forrest, K. A.; Furukawa, H.; Eckert, J.; Space, B. Hydrogen Adsorption in a Zeolitic Imidazolate Framework with Its Topology. *J. Phys. Chem. C* **2018**, *122*, 15435–15445.
- (11) Zhang, Y.-B.; Furukawa, H.; Ko, N.; Nie, W.; Park, H. J.; Okajima, S.; Cordova, K. E.; Deng, H.; Kim, J.; Yaghi, O. M. Introduction of Functionality, Selection of Topology, and Enhancement of Gas Adsorption in Multivariate Metal-Organic Framework-177. *J. Am. Chem. Soc.* **2015**, *137*, 2641–2650.
- (12) Yan, Y.; Silva, I. D.; Blake, A. J.; Daily, A.; Manuel, P.; Yang, S.; Schroder, M. High Volumetric Hydrogen Adsorption in a Porous Anthracene-Decorated Metal-Organic Framework. *Inorg. Chem.* **2018**, *57*, 12050–12055.
- (13) Jiang, J.; Furukawa, H.; Zhang, Y.-B.; Yaghi, O. M. High Methane Storage Working Capacity in Metal-Organic Frameworks with Acrylate Links. *J. Am. Chem. Soc.* **2016**, *138*, 10244–10251.
- (14) Yan, Y.; Kolokolov, D. I.; Silva, I. D.; Stepanov, A. G.; Blake, A. J.; Dailly, A.; Manuel, P.; Tang, C. C.; Yang, S.; Schroder, M. Porous Metal-Organic Polyhedral Frameworks with Optimal Molecular Dynamics and Pore Geometry for Methane Storage. *J. Am. Chem. Soc.* **2017**, *139*, 13349–13360.
- (15) Mason, J. A.; Oktawiec, J.; Taylor, M. K.; Hudson, M. R.; Rodriguez, J.; Bachman, J. E.; Gonzalez, M. I.; Cervellino, A.; Guagliardi, A.; Brown, C. M.; Llewellyn, P. L.; Masciocchi, N.; Long, J. R. Methane Storage in Flexible Metal-Organic Frameworks with Intrinsic Thermal Management. *Nature* **2015**, *527*, 357–361.
- (16) Wen, H.-M.; Li, B.; Li, L.; Lin, R.-B.; Zhou, W.; Qian, G.; Chen, B. A Metal-Organic Framework with Optimized Porosity and Functional Sites for High Gravimetric and Volumetric Methane Storage Working Capacities. *Adv. Mater.* **2018**, *30*, 1704792–1704798.
- (17) Tian, T.; Zeng, Z.; Vulpe, D.; Casco, M. E.; Divitini, G.; Midgley, P. A.; Silvestre-Albero, J.; Tan, J.-C.; Moghadam, P. Z.; Fairen-Jimenez, D. A sol-gel monolithic metal-organic framework with enhanced methane uptake. *Nat. Mater.* **2018**, *17*, 174–180.
- (18) Connolly, B. M.; Aragonés-Anglada, M.; Gandara-Loe, J.; Dana, N. A.; Lamb, D. C.; Mehta, J. P.; Vulpe, D.; Wuttke, S.; Silvestre-Albero, J.; Moghadam, P. Z.; Wheatley, A. E. H.; Fairen-Jimenez, D. Tuning porosity in macroscopic monolithic metal-organic frameworks for exceptional natural gas storage. *Nat. Commun.* **2019**, *10*, DOI: 10.1038/s41467-019-10185-1.
- (19) Tranchemontagne, D. J.; Ni, Z.; O’Keeffe, M.; Yaghi, O. M. Reticular Chemistry of Metal-Organic Polyhedra. *Angew. Chem., Int. Ed.* **2008**, *47*, 5136–5147.
- (20) Zhao, D.; Yuan, D.; Krishna, R.; Van Baten, J. M.; Zhou, H.-C. Thermosensitive Gating Effect and Selective Gas Adsorption in a Porous Coordination Nanocage. *Chem. Commun.* **2010**, *46*, 7352–7354.
- (21) Murase, T.; Nishijima, Y.; Fujita, M. Cage-Catalyzed Knoevenagel Condensation Under Neutral Conditions in Water. *J. Am. Chem. Soc.* **2012**, *134*, 162–164.
- (22) Zhang, J.-H.; Xie, S.-M.; Wang, B.-J.; He, P.-G.; Yuan, L.-M. Highly Selective Separation of Enantiomers Using a Chiral Porous Organic Cage. *J. Chromatogr. A* **2015**, *1426*, 174–182.
- (23) Jiao, Y.; Zhang, J.; Zhang, L.; Lin, Z.; He, C.; Duan, C. Metal-Organic Polyhedra Containing 36 and 24 Folds of Amide Groups For Selective Luminescent Recognition of Natural Disaccharides. *Chem. Commun.* **2012**, *48*, 6022–6024.
- (24) Giri, N.; Del Popolo, M. G.; Melaugh, G.; Greenaway, R. L.; Ratzke, K.; Koschine, T.; Pison, L.; Costa Gomes, M. F.; Cooper, A. I.; James, S. L. Liquids With Permanent Porosity. *Nature* **2015**, *527*, 216–220.
- (25) Cooper, A. I. Porous Molecular Solids and Liquids. *ACS Cent. Sci.* **2017**, *3*, 544–553.
- (26) Mastalerz, M. Porous Shape-Persistent Organic Cage Compounds of Different Size, Geometry, and Function. *Acc. Chem. Res.* **2018**, *51*, 2411–2422.
- (27) Flippen, J. L.; Karle, J.; Karle, I. L. The Crystal Structure of a Versatile Organic Clathrate. 4-*p*-Hydroxyphenyl-2,2,4-trimethylchroman (Dianin’s Compound). *J. Am. Chem. Soc.* **1970**, *92*, 3749–3754.
- (28) Koifman, O. I.; Mamardashvili, N. Zh.; Surov, O. V. Porous Molecular Crystals of Calix[4]arenes. *Russ. Chem. Bull.* **2017**, *66*, 241–253.
- (29) Lim, S.; Kim, H.; Selvapalam, N.; Kim, K.-J.; Cho, S. J.; Seo, G.; Kim, K. Cucurbit[6]uril: Organic Molecular Porous Material With Permanent Porosity, Exceptional Stability, and Acetylene Sorption Properties. *Angew. Chem., Int. Ed.* **2008**, *47*, 3352–3355.
- (30) Tian, J.; Thallapally, P. K.; Dalgarno, S. J.; McGrail, P. B.; Atwood, J. L. Amorphous Molecular Organic Solids for Gas Adsorption. *Angew. Chem., Int. Ed.* **2009**, *48*, 5492–5495.
- (31) Bezzu, C. G.; Hellowell, M.; Warren, J. E.; Allen, D. R.; McKeown, N. B. Heme-Like Coordination Chemistry Within Nanoporous Molecular Crystals. *Science* **2010**, *327*, 1627–1630.
- (32) Christinat, N.; Scopelliti, R.; Severin, K. Multicomponent Assembly of Boronic Acid Based Macrocycles and Cages. *Angew. Chem., Int. Ed.* **2008**, *47*, 1848–1852.
- (33) Lee, S.; Yang, A.; Moneypenny, T. P.; Moore, J. S. Kinetically Trapped Tetrahedral Cages via Alkyne Metathesis. *J. Am. Chem. Soc.* **2016**, *138*, 2182–2185.
- (34) Tozawa, T.; Jones, J. T. A.; Swamy, S. L.; Adams, D. J.; Shakespeare, S.; Clowes, R.; Bradshaw, D.; Hasell, T.; Chong, S. Y.; Tang, C.; Thompson, S.; Parker, J.; Trewin, A.; Bacsá, J.; Slawin, A. M. Z.; Steiner, A.; Cooper, A. I. Porous Organic Cages. *Nat. Mater.* **2009**, *8*, 973–978.
- (35) Ni, Z.; Yassar, A.; Antoun, T.; Yaghi, O. M. Porous Metal-Organic Truncated Octahedron Constructed from Paddle-Wheel Squares and Terthiophene Links. *J. Am. Chem. Soc.* **2005**, *127*, 12752–12753.
- (36) Furukawa, H.; Kim, J.; Ockwig, N. W.; O’Keeffe, M.; Yaghi, O. M. Control of Vertex Geometry, Structure Dimensionality, Functionality, and Pore Metrics in the Reticular Synthesis of Crystalline Metal-Organic Frameworks and Polyhedra. *J. Am. Chem. Soc.* **2008**, *130*, 11650–11661.
- (37) Boer, S. A.; White, K. F.; Slater, B.; Emerson, A. J.; Knowles, G. P.; Donald, W. A.; Thornton, A. W.; Ladewig, B. P.; Bell, T. D. M.; Hill, M. R.; Chaffee, A. L.; Abrahams, B. F.; Turner, D. R. A Multifunctional, Charge-Neutral, Chiral Octahedral $M_{12}L_{12}$ Cage. *Chem. - Eur. J.* **2019**, *25*, DOI: 10.1002/chem.201901681.
- (38) Yan, Y.; Yang, S.; Blake, A. J.; Schroder, M. Studies on Metal-Organic Frameworks of Cu(II) with Isophthalate Linkers for Hydrogen Storage. *Acc. Chem. Res.* **2014**, *47*, 296–307.
- (39) Eddaoudi, M.; Kim, J.; Wachter, J. B.; Chae, H. K.; O’Keeffe, M.; Yaghi, O. M. Porous Metal-Organic Polyhedra: 25 Å Cuboctahedron Constructed from 12 $Cu_2(CO_2)_4$ Paddle-Wheel Building Blocks. *J. Am. Chem. Soc.* **2001**, *123*, 4368–4369.
- (40) Ke, Y.; Collins, D. J.; Zhou, H.-C. Synthesis and Structure of Cuboctahedral and Anticuboctahedral Cages Containing 12 Quadruply Bonded Dimolybdenum Units. *Inorg. Chem.* **2005**, *44*, 4154–4156.
- (41) Young, M. D.; Zhang, Q.; Zhou, H.-C. Metal-organic polyhedra constructed from dinuclear ruthenium paddlewheels. *Inorg. Chim. Acta* **2015**, *424*, 216–220.
- (42) Furukawa, S.; Horike, N.; Kondo, M.; Hijikata, Y.; Carne-Sanchez, A.; Larpent, P.; Louvain, N.; Diring, S.; Sato, H.; Matsuda, R.; Kawano, R.; Kitagawa, S. Rhodium-Organic Cuboctahedra as Porous Solids with Strong Binding Sites. *Inorg. Chem.* **2016**, *55*, 10843–10846.

- (43) Park, J.; Perry, Z.; Chen, Y.-P.; Bae, J.; Zhou, H.-C. Chromium(II) Metal-Organic Polyhedra as Highly Porous Materials. *ACS Appl. Mater. Interfaces* **2017**, *9*, 28064–28068.
- (44) Gosselin, E. J.; Rowland, C. A.; Balto, K. P.; Yap, G. P. A.; Bloch, E. D. Design and Synthesis of Porous Nickel(II) and Cobalt(II) Cages. *Inorg. Chem.* **2018**, *57*, 11847–11850.
- (45) Lorzing, G. R.; Trump, B. A.; Brown, C. M.; Bloch, E. D. Selective Gas Adsorption in Highly Porous Chromium(II)-Based Metal-Organic Polyhedra. *Chem. Mater.* **2017**, *29*, 8583–8587.
- (46) Chiu, S. S.-Y.; Lo, S. M.-F.; Charmant, J. P. H.; Orpen, A. G.; Williams, I. D. A. Chemically Functionalizable Nanoporous Material $[\text{Cu}_3(\text{TMA})_2(\text{H}_2\text{O})]_n$. *Science* **1999**, *283*, 1148–1150.
- (47) Wade, C. R.; Dinca, M. Investigation of the synthesis, activation, and isosteric heats of CO_2 adsorption of the isostructural series of metal-organic frameworks $\text{M}_3(\text{BTC})_2$ ($\text{M} = \text{Cr}, \text{Fe}, \text{Ni}, \text{Cu}, \text{Mo}, \text{Ru}$). *Dalton Trans* **2012**, *41*, 7931–7938.
- (48) Wang, X.-S.; Ma, S.; Rauch, K.; Simmons, J. M.; Yuan, D.; Wang, X.; Yildirim, T.; Cole, W. C.; Lopez, J. J.; de Meijere, A.; Zhou, H.-C. Metal-Organic Frameworks Based on Double-Bond-Coupled Di-Isophthalate Linkers with High Hydrogen and Methane Uptakes. *Chem. Mater.* **2008**, *20*, 3145–3152.
- (49) Wang, X.-S.; Ma, S.; Forster, P. M.; Yuan, D.; Eckert, J.; Lopez, J. J.; Murphy, B. J.; Parise, J. B.; Zhou, H.-C. Enhancing H_2 Uptake by “Close-Packing” Alignment of Open Copper Sites in Metal-Organic Frameworks. *Angew. Chem., Int. Ed.* **2008**, *47*, 7263–7266.
- (50) Yuan, D.; Zhao, D.; Sun, D.; Zhou, H.-C. An Isoreticular Series of Metal-Organic Frameworks with Dendritic Hexacarboxylate Ligands and Exceptionally High Gas-Uptake Capacity. *Angew. Chem., Int. Ed.* **2010**, *49*, 5357–5361.
- (51) Yan, Y.; Lin, X.; Yang, S.; Blake, A. J.; Dailly, A.; Champness, N. R.; Hubberstey, P.; Schröder, M. Exceptionally high H_2 storage by a metal-organic polyhedral framework. *Chem. Commun.* **2009**, 1025–1027.
- (52) Yan, Y.; Blake, A. J.; Lewis, W.; Barnett, S. A.; Dailly, A.; Champness, N. R.; Schröder, M. Modifying Cage Structures in Metal-Organic Polyhedral Frameworks for H_2 Storage. *Chem. - Eur. J.* **2011**, *17*, 11162–11170.
- (53) Yan, Y.; Suyetin, M.; Bichoutskaia, E.; Blake, A. J.; Allan, D. R.; Barnett, S. A.; Schröder, M. Modulating the packing of $[\text{Cu}_2(\text{isophthalate})_{24}]$ cuboctahedra in a triazole-containing metal-organic polyhedral framework. *Chem. Sci.* **2013**, *4*, 1731–1736.
- (54) Wilmer, C. E.; Farha, O. K.; Yildirim, T.; Eryazici, I.; Krungleviciute, V.; Sarjeant, A. A.; Snurr, R. Q.; Hupp, J. T. Gram-scale, high-yield synthesis of a robust metal-organic framework for storing methane and other gases. *Energy Environ. Sci.* **2013**, *6*, 1158–1163.
- (55) Yan, Y.; Telepeni, I.; Yang, S.; Lin, X.; Kockelmann, W.; Dailly, A.; Blake, A. J.; Lewis, M.; Walker, G. S.; Allan, D. R.; Barnett, S. A.; Champness, N. R.; Schröder, M. Metal-Organic Polyhedral Frameworks: High H_2 Adsorption Capacities and Neutron Powder Diffraction Studies. *J. Am. Chem. Soc.* **2010**, *132*, 4092–4094.
- (56) Yan, Y.; Kolokolov, D. I.; Silva, I. D.; Stepanov, A. G.; Blake, A. J.; Dailly, A.; Manuel, P.; Tang, C. C.; Yang, S.; Schroder, M. Porous Metal-Organic Polyhedral Frameworks with Optimal Molecular Dynamics and Pore Geometry for Methane Storage. *J. Am. Chem. Soc.* **2017**, *139*, 13349–13360.
- (57) Gosselin, E. J.; Lorzing, G. R.; Trump, B. A.; Brown, C. M.; Bloch, E. D. Gas adsorption in an isostructural series of pillared coordination cages. *Chem. Commun.* **2018**, *54*, 6392–6395.
- (58) Wang, C.-H.; Das, A.; Gao, W.-Y.; Powers, D. C. Probing Substrate Diffusion in Interstitial MOF Chemistry with Kinetic Isotope Effects. *Angew. Chem., Int. Ed.* **2018**, *57*, 3676–3681.
- (59) Apex3; Bruker AXS Inc.: Madison, WI, 2015.
- (60) Sheldrick, G. M. SHELXT - Integrated space-group and crystal-structure determination. *Acta Crystallogr., Sect. A: Found. Adv.* **2015**, *A71*, 3–8.
- (61) Sheldrick, G. M. Crystal structure refinement with SHELXL. *Acta Crystallogr., Sect. C: Struct. Chem.* **2015**, *C71*, 3–8.
- (62) Spek, A. L. PLATON SQUEEZE: a tool for the calculation of the disordered solvent contribution to the calculated structure factors. *Acta Crystallogr., Sect. C: Struct. Chem.* **2015**, *C71*, 9–18.
- (63) Coelho, A. *Topas Academic V6*; Coelho Software, 2017.
- (64) Chun, H.; Jung, H.; Seo, J. Isoreticular Metal-Organic Polyhedral Networks Based on 5-Connecting Paddlewheel Motifs. *Inorg. Chem.* **2009**, *48*, 2043–2047.
- (65) Pawley, G. S. Unit-Cell Refinement from Powder Diffraction Scans. *J. Appl. Crystallogr.* **1981**, *14*, 357–361.
- (66) Andreev, Y. G.; MacGlashan, G. S.; Bruce, P. G. Ab Initio Solution of a Complex Crystal Structure from Powder-Diffraction Data Using Simulated-Annealing Method and a High Degree of Molecular Flexibility. *Phys. Rev. B: Condens. Matter Mater. Phys.* **1997**, *55*, 12011–12017.
- (67) Toby, B. H. EXPGUI, a Graphical User Interface for GSAS. *J. Appl. Crystallogr.* **2001**, *34*, 210–213.
- (68) Hulvey, Z.; Vlaisavljevich, B.; Mason, J. A.; Tsivion, E.; Dougherty, T. P.; Bloch, E. D.; Head-Gordon, M.; Smit, B.; Long, J. R.; Brown, C. M. Critical Factors Driving the High Volumetric Uptake of Methane in $\text{Cu}_3(\text{Btc})_2$. *J. Am. Chem. Soc.* **2015**, *137*, 10816–10825.
- (69) Rowland, C. A.; Lorzing, G. R.; Gosselin, E. J.; Trump, B. A.; Yap, G. P. A.; Brown, C. M.; Bloch, E. D. Methane Storage in Paddlewheel-Based Porous Coordination Cages. *J. Am. Chem. Soc.* **2018**, *140*, 11153–11157.
- (70) Weller, M. T.; Henry, P. F.; Ting, V. P.; Wilson, C. C. Crystallography of Hydrogen-Containing Compounds: Realizing the Potential of Neutron Powder Diffraction. *Chem. Commun.* **2009**, 7345, 2973.
- (71) Wilson, C. C.; Henry, P. F.; Schmidtman, M.; Ting, V. P.; Williams, E.; Weller, M. T. Neutron Powder Diffraction-New Opportunities in Hydrogen Location in Molecular and Materials Structure. *Crystallogr. Rev.* **2014**, *20*, 162–206.
- (72) Kapelewski, M. T.; Geier, S. J.; Hudson, M. R.; Stück, D.; Mason, J. A.; Nelson, J. N.; Xiao, D. J.; Hulvey, Z.; Gilmour, E.; FitzGerald, S. A.; Head-Gordon, M.; Brown, C. M.; Long, J. R. $\text{M}_2(m\text{-dobdc})$ ($\text{M} = \text{Mg}, \text{Mn}, \text{Fe}, \text{Co}, \text{Ni}$) Metal-Organic Frameworks Exhibiting Increased Charge Density and Enhanced H_2 Binding at the Open Metal Sites. *J. Am. Chem. Soc.* **2014**, *136*, 12119–12129.
- (73) <https://github.com/SimonEnsemble/BlochCages>.
- (74) Martin, M. G.; Siepmann, J. I. Transferable Potentials for Phase Equilibria. I. United-Atom Description of n -Alkanes. *J. Phys. Chem. B* **1998**, *102*, 2569–2577.
- (75) Mayo, S. L.; Olafson, B. D.; Goddard, W. A. DREIDING: A Generic Force Field for Molecular Simulations. *J. Phys. Chem.* **1990**, *94*, 8897–8909.
- (76) Rappe, A. K.; Casewit, C. J.; Colwell, K. S.; Goddard, W. A.; Skiff, W. M. UFF, a full periodic table force field for molecular mechanics and molecular dynamics simulations. *J. Am. Chem. Soc.* **1992**, *114*, 10024–10035.
- (77) Childs, H.; Brugger, E.; Whitlock, B.; Meredith, J.; Ahern, S.; Pugmire, D.; Biagas, K.; Miller, M.; Harrison, C.; Weber, G. H.; Krishnan, H.; Fogal, T.; Sanderson, A.; Garth, C.; Bethel, E. W.; Camp, D.; Rubel, O.; Durant, M.; Favre, J. M.; Navratil, P. VisIt: An End-User Tool for Visualizing and Analyzing Very Large Data. *High Performance Visualization-Enabling Extreme-Scale Scientific Insight* **2012**, 20124456, 357–372.
- (78) Frenkel, D.; Smit, B. *Understanding Molecular Simulation: From Algorithms to Applications*; Academic Press: Harcourt, 1996.
- (79) Li, J.-R.; Yakovenko, A. A.; Lu, W.; Timmons, D. J.; Zhuang, W.; Yuan, D.; Zhou, H.-C. Ligand Bridging-Angle-Driven Assembly of Molecular Architectures Based on Quadruply Bonded Mo-Mo Dimers. *J. Am. Chem. Soc.* **2010**, *132*, 17599–17610.
- (80) Cotton, F. A.; Hillard, E. A.; Murillo, C. A.; Zhou, H.-C. After 155 Years, A Crystalline Chromium Carboxylate with a Supershort Cr-Cr Bond. *J. Am. Chem. Soc.* **2000**, *122*, 416–417.
- (81) Mason, J. A.; Veenstra, M.; Long, J. R. Evaluating metal-organic frameworks for natural gas storage. *Chem. Sci.* **2014**, *5*, 32–51.